Article

Anatomy of a Paroxysmal Lava Fountain at Etna Volcano: The Case of the 12 March 2021, Episode

Sonia Calvari * , **Alessandro Bonaccorso** and **Gaetana Ganci**

Istituto Nazionale di Geofisica e Vulcanologia, Osservatorio Etneo-Sezione di Catania, 95125 Catania, Italy; alessandro.bonaccorso@ingv.it (A.B.); gaetana.ganci@ingv.it (G.G.)
* Correspondence: sonia.calvari@ingv.it

Abstract: On 13 December 2020, Etna volcano entered a new eruptive phase, giving rise to a number of paroxysmal episodes involving increased Strombolian activity from the summit craters, lava fountains feeding several-km high eruptive columns and ash plumes, as well as lava flows. As of 2 August 2021, 57 such episodes have occurred in 2021, all of them from the New Southeast Crater (NSEC). Each paroxysmal episode lasted a few hours and was sometimes preceded (but more often followed) by lava flow output from the crater rim lasting a few hours. In this paper, we use remote sensing data from the ground and satellite, integrated with ground deformation data recorded by a high precision borehole strainmeter to characterize the 12 March 2021 eruptive episode, which was one of the most powerful (and best recorded) among that occurred since 13 December 2020. We describe the formation and growth of the lava fountains, and the way they feed the eruptive column and the ash plume, using data gathered from the INGV visible and thermal camera monitoring network, compared with satellite images. We show the growth of the lava flow field associated with the explosive phase obtained from a fixed thermal monitoring camera. We estimate the erupted volume of pyroclasts from the heights of the lava fountains measured by the cameras, and the erupted lava flow volume from the satellite-derived radiant heat flux. We compare all erupted volumes (pyroclasts plus lava flows) with the total erupted volume inferred from the volcano deflation recorded by the borehole strainmeter, obtaining a total erupted volume of ~3 × 10^6 m^3 of magma constrained by the strainmeter. This volume comprises ~1.6 × 10^6 m^3 of pyroclasts erupted during the lava fountain and 2.4 × 10^6 m^3 of lava flow, with ~30% of the erupted pyroclasts being remobilized as rootless lava to feed the lava flows. The episode lasted 130 min and resulted in an eruption rate of ~385 m^3 s^{-1} and caused the formation of an ash plume rising from the margins of the lava fountain that rose up to 12.6 km a.s.l. in ~1 h. The maximum elevation of the ash plume was well constrained by an empirical formula that can be used for prompt hazard assessment.

Keywords: Etna volcano; paroxysmal explosive and effusive episodes; ash plume; remote sensing; volcano monitoring; volcanic hazard

1. Introduction

Explosive eruptions of mafic magmas produce lava fountains whose heights depend on the exsolved volatile content of the magma, its erupted mass flux, and the geometry of the vent, either an elongated eruptive fissure or a near circular conduit [1]. Lava fountains were typical at Kilauea volcano during the 1959–1960, 1969–1970, and 1983–2008 eruptions [2–5], being characterized by vertical jets of gas and incandescent pyroclasts rising several hundred meters above the vent. This activity is also common at Etna volcano, with several such explosive phases occurring in 2000 [6–8], 2001, 2002–2003 [9–11], and in 2011–2015 [12–16]. The last paroxysmal lava fountain sequence started on 13 December 2020, and is still going on as of 2 August 2021. A recent study, based on a catalogue of the explosive paroxysmal episodes that occurred at Etna since 1986 (and updated to 1 April 2021), showed a general marked increase in the release of seismic energy

over time [17]. This is in agreement with a general trend of increasing heights and volume of the lava fountains and ash plumes from 2000 until now [6,8,10–12,14,15].

The summit of Etna volcano comprises four main craters: Voragine, Bocca Nuova, NE Crater, and SE Crater, with the addition of the newly formed New SE Crater (NSEC) built up on top of the SE Crater since 2011 [14,18]. Lava fountains from the summit craters or from eruptive fissures have often preceded major flank effusive activity, such as at Etna in 2001 and 2002–2003; thus, they were considered as possible precursors [10,11]. However, the several lava fountain events between 2011 and 2015 [12,14–17,19] were not followed by flank eruptions. This observation, combined with the estimation of erupted volumes from the monitoring camera analyses [14,15], allowed recognizing that Etna displayed a steady-state behavior for at least four decades [20–23]. Therefore, in cases such as the 2011–2015 lava fountains, this explosive activity can represent a modality of magma discharge able to maintain the steady-state. At Etna volcano, the average output rate was estimated at 0.8 $m^3 s^{-1}$, or 25×10^6 m^3 per year [21,22]. On this basis, Bonaccorso and Calvari [22] found that the magma stored within the plumbing system can be released either through a high number of lava fountains, erupting volumes of ~2–3 $\times 10^6$ m^3 each [12,14,15,22], or with a small number of flank effusive eruptions, each normally releasing ~30–60 $\times 10^6$ m^3 of lava [21,22]. Considering this conceptual model, it is not surprising that on 13 December 2020, after about 18 months of eruptive pause [24–27], the volcano entered a new eruptive phase characterized by 57 lava fountain episodes (as of 2 August 2021) accompanied, preceded, or followed by short-lasting effusive phases. Lava fountains, being characterized at Etna by heights of a few km, and always accompanied by several km high ash plumes generated from the same vent, raise serious concern among the local population. In fact, an ash fallout up to ~38 kg/m^2 [10] has a strong impact on the viability, on the stability of roofs, on the air traffic (the Catania airport is a major international hub), on agriculture, on water contamination, and on the health of the local population [28–32].

The release of ash plumes during mild basaltic explosive activity was described and analyzed only recently, when two distinct eruption styles were identified for Strombolian explosions [33]. Type 1 Strombolian eruptions consist of coarse ballistic scoria (cm/dm-scale) and a relatively ash-free gas plume. Type 2 Strombolian eruptions consist of an ash-rich plume, with or without additional ballistic scoria. What determines type 2 ash-rich Strombolian behavior is the sliding of loose clastic material into the vent [33–35], or rheological changes in the uppermost magma column [36,37]. The formation of ash plume during lava fountaining is even more questioned and often not considered in lava fountain models [38,39]. This is because lava fountaining is considered as mostly characterized by coarse ballistics falling around the vent and building spatter cones or spatter ramparts, with small amounts of ash being released in the atmosphere [40–42].

The formation of ash plumes is a common feature at Etna volcano, always accompanying lava fountain eruptions [6–15,17]. Conversely, ash plume is lacking during Strombolian and intermediate explosive activity [43], but is released by the summit craters during rare phreatomagmatic activity [44–46]. In addition, weak and dilute ash plume may form during summit collapses, occurring within the craters or pit crater formations [44,47,48].

Several authors described a transitional explosive stage in between the Strombolian and lava fountain [6,14,39,43], occurring when the discrete countable Strombolian bursts increase in number and frequency, shifting to the continuous lava fountaining regime [14,43]. This transition can be either abrupt or gradual [6]. At Etna, lava fountains are always associated to the formation of ash plumes [6,7,10,11,14,15], and as soon as the lava fountain regime starts, we observe the release of ash from the upper part of the lava fountain that rises for kilometers above the crater, feeding a sustained ash plume [42]. However, the way a lava fountain expands vertically into a sustained ash plume, as well as the timing of this process, is still little constrained. Nonetheless, sustained eruptive columns and ash plumes are of great concern to local authorities in Sicily and elsewhere [17,49–51] because the ash plumes may expand well beyond the national country. As an example, Etna's ash plumes also affected Malta and Greece [25,45,52,53] for several days after the

end of the eruption [54], and its gas and ash plumes even travelled the entire globe [55]. Even worse, the eruption of Mt St Helens in 1982 [49], Pinatubo in 1991 [56], and the Icelandic volcano Eyjafjallajökull in 2010 caused air traffic disruption for about a month across Europe [50,51].

In this paper, we have analyzed, in detail, one of the most powerful (and best recorded) lava fountains taking place between 13 December 2020, and 20 July 2021, namely the episode of 12 March 2021, which occurred during good weather conditions and in the daytime (Figure 1), and enabled the collection of excellent data from the ground and satellite. We present details on the lava fountains and their connections with ash plume and lava flow field formation, as well as persistence and decline gathered from a network of ground-based monitoring cameras and from high temporal resolution satellite sensors (e.g., SEVIRI, MODIS, and VIIRS). We compare the timing and volumes obtained from these devices with results from the reference borehole strainmeter [57,58], in order to highlight key processes that characterize the phenomenon and are useful for hazard assessment. In particular, we analyze the formation and growth of the lava fountain and of the associated lava flow field, the timing, and how the fountain feeds the ash column and eruptive plume. Our focus was to acquire parameters that could be useful for prompt hazard assessment.

Figure 1. Photo of Etna paroxysmal episode on 12 March 2021. The shot was taken at 08:50 UTC from the main road (Etnea Street) crossing N–S the city of Catania. The view is from south (photo by A.B.).

2. Methods

2.1. Camera Networks

We used the monitoring camera network installed and maintained by the Istituto Nazionale di Geofisica e Vulcanologia (INGV) Osservatorio Etneo-Sezione di Catania, comprising thermal and visible cameras, in order to detect and quantify the phases of

eruptive activity. Our aim was to define the timing of its changes, as well as the height of the lava fountains and ash plume, the erupted volume of pyroclastics and the expansion of the lava flow field, and of their timing—parameters that are essential for hazard assessment at a frequently erupting volcano. The labels of the cameras used in this paper, as well as their main features, viewing direction, and average distance from the craters, are listed in Table 1, and their positions are shown in Figure 2. The height of the lava fountains was obtained from the thermal cameras ENT and EBT located on the S and NW flanks of the volcano, respectively. The error in the height measurement is ±50 m [14,15]. These heights were used to calculate the erupted volume of pyroclasts, following the method developed by Calvari et al. [14,15]. This method consists in measuring the lava fountain height on thermal images with a 1-minute time lapse, and applying the Equation (1):

$$v = (2gh)^{0.5} \tag{1}$$

for the calculation of the flux of gas and pyroclasts through the vent section. In Equation (1), v is the velocity of the mixture comprising gas plus pyroclasts, g is the acceleration of gravity, and h is the lava fountain height, expressed in meters above the crater rim. The NSEC vent section, following Calvari et al. [14,15], was considered circular, with a vent diameter of 30 m. By integrating the velocity of the gas plus pyroclasts mixture over the entire duration of the lava fountain, multiplied by the vent section area, and extracting from the final value the 0.18%, which represents the average amount of pyroclasts within the fluid mixture [14,15], we obtain the volume of pyroclasts erupted during the lava fountain episode. It is worth noting that the growth of the NSEC cinder cone during one single lava fountain episode is not enough to affect our measurements of lava fountain or ash plumes [18].

Table 1. List of the INGV monitoring cameras used in this paper and their main features. The field of view is considered at the crater rim.

| Label	Type	Location	Distance from the Craters (km)	Frame Rate	Field of View
ENT	Thermal FLIR A40M	Nicolosi, South flank 730 m a.s.l.	15.0	2 frames/s	24° (horizontal) 18° (vertical)
EBT	Thermal FLIR A320	Bronte, NW flank 85 m a.s.l.	13.5	2 frames/s	25° (horizontal) 18.8° (vertical)
EMCT	Thermal FLIR A320	Mt. Cagliato, East flank 1160 m a.s.l.	8.3	2 frames/s	25° (horizontal) 18.8° (vertical)
EMOT	Thermal FLIR A320	Montagnola, South flank 2600 m a.s.l.	3.0	1 frame/s	25° (horizontal) 18.8° (vertical)
EMCH	Visible Vivotec IP8172	Mt. Cagliato, East flank 390 m a.s.l.	8.3	2 frames/min	33°~93° (horizontal), 24°~68° (vertical)
ECV	Visible Canon VC-C4R	Catania Nesima, South flank 35 m a.s.l.	26.7	1 frame/2 s	3–47.5° (horizontal and vertical)
ECVH	Visible Vivotec IP8172	Catania Nesima, South flank 35 m a.s.l.	27.0	1 frame/min	33°~93° (horizontal), 24°~68° (vertical)
EBVH	Visible Vivotec IP8172	Bronte, NW flank 163 m a.s.l.	13.5	1 frame/min	33°~93° (horizontal), 24°~68° (vertical)
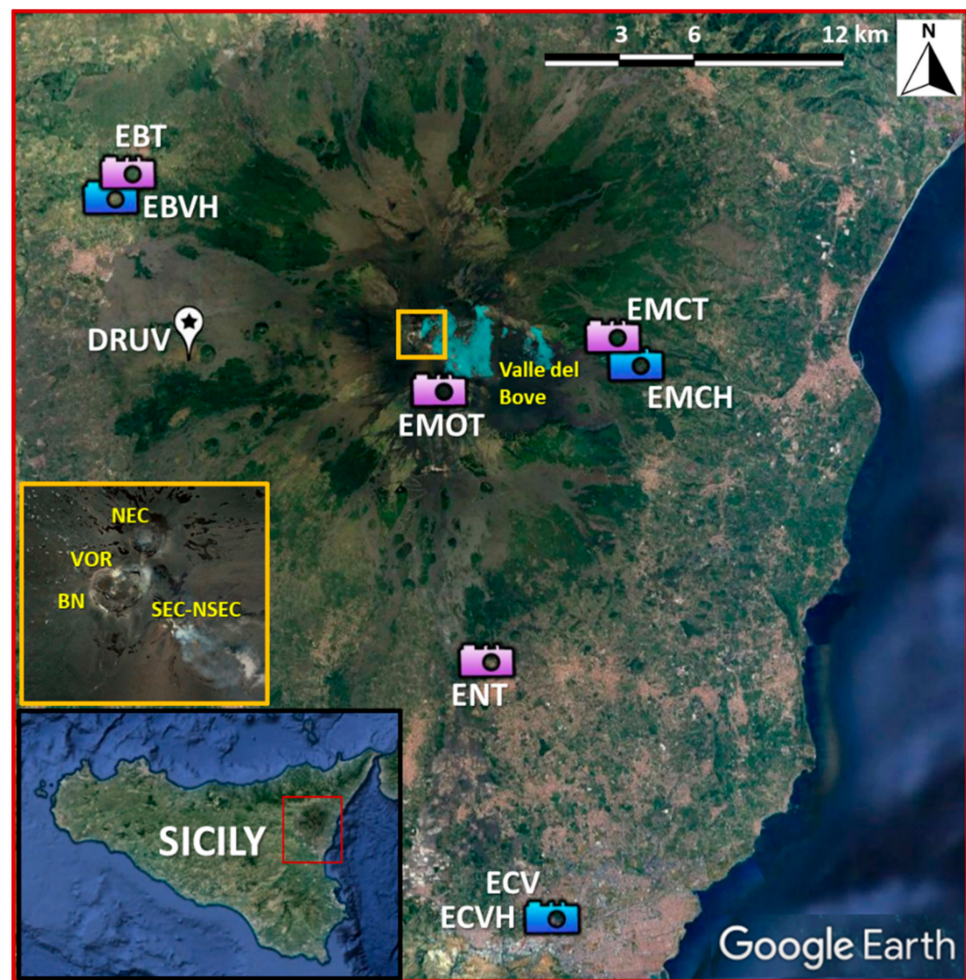
Figure 2. Map of INGV monitoring cameras and borehole strainmeter (DRUV) used in this paper. The pale blue area shows the portion of topography that can be imaged by the EMCT and EMCH cameras, used for the emplacement of the 12 March 2021, lava flow field. The Northeast Crater (NEC), Voragine (VOR), Bocca Nuova (BN), Southeast Crater (SEC), and New Southeast Crater (NSEC) summit craters are indicated in the yellow frame inset. The blue color is for visible cameras, the purple color is for thermal cameras.

The height of the ash plume was measured from the calibrated [59–61] visible cameras ECV and EBVH located on the S and NW flank of the volcano, respectively. ECV has a maximum vertical field of view of ~9.0–9.5 km above sea level (a.s.l.), whereas EBVH allows the detection of ash plumes up to ~12.5 km a.s.l., depending on the wind speed and direction [59–61].

The EMCT thermal camera (Table 1 and Figure 2) was used to follow the lava flow emplacement associated with the lava fountaining activity [62,63]. This camera is located ~8.3 km east of the summit craters (Figure 2, Table 1). Thermal images acquired from EMCT are currently received in real time and stored as RGB files. A routine was implemented to automatically process the images. The images are reprojected on the topography, considering the position and orientation of the camera. To detect the active portion of the lava flow, a threshold is set at 245 for the red channel. This threshold was found by considering the histogram images of recorded values in the presence—or not—of lava flow. Concerning the topography, a digital elevation model derived from Pleiades images and updated in 2020 is taken into account.

2.2. Satellite Thermal Monitoring

Low spatial-high temporal resolution satellite images (1–3 km pixel at nadir, 6 h—up to 5 min frequency), such as those acquired by SEVIRI, MODIS, and VIIRS, are currently used to follow the eruptive activity at Mount Etna. Due to the short-lived nature of the lava fountains that occurred to date in 2021, SEVIRI aboard the geostationary Meteosat Second Generation, providing information at 15 to 5 min sample times, is the best sensor to describe the evolution of the eruptive phenomena [62,64,65]. The thermal anomalies related to the volcanic activity can be located in the satellite images by processing the middle infrared (MIR) channel that is particularly sensitive to high temperature events. The automatic system HOTSAT [66] was used to process these data. Besides locating the thermal anomalies, HOTSAT also computes the radiant heat flux by quantifying the thermal anomaly in each image. From a temporal sequence of images, a radiant heat flux curve can be retrieved, and the timing of an eruptive event can be determined. In the case of effusive events, this curve can provide an estimation of the eruption rate, i.e., it can be converted into a time averaged discharge rate (TADR; [64,67–69]), TADR being an essential parameter for defining the size and magnitude of a volcanic eruption [40,68]. This conversion entails some assumptions [70], among which the thermal steady state needs to be reached [71]. Lava fountains are very fast and transient events, so converting the radiant heat flux into TADR is not possible. Indeed, during the climax phase, saturation and plume obscuration occur, increasing the uncertainties on the peak values of radiant heat flux. To overcome these limitations, the method developed by Ganci et al. [65] was applied here. This method considers the surface temperature for a stagnant, stable, cooling lava surface as a function of time following the solution of the Stefan cooling problem [68,72]. The satellite-derived radiant heat flux depends on the radiative heat flux density due to the surface temperature and the area of cooling lava. The erupted volume of lava is hence computed by modeling the cooling curve apparent in the satellite-derived radiant heat flux curve. A minimum and a maximum range of thickness are assumed for the lava flow field, and the actual curve is constrained between two modeled curves by using the Nelder–Mead algorithm.

SEVIRI, MODIS, and VIIRS data were also used to compute the volcanic Ash Cloud Top Height (ACTH). In this work, this value was derived by comparing the brightness temperature for the pixels contaminated by the volcanic plume with atmospheric temperature profiles. Data for the atmospheric profiles were downloaded with hourly frequency, regridded to a regular lat–long grid of 0.25 degrees, from ERA5, the fifth generation ECMWF reanalysis for the global climate and weather (available at https://cds.climate.copernicus.eu/, accessed on 2 August 2021). The radiances acquired in the thermal infrared were corrected for atmospheric effect by using the MODTRAN (MODerate resolution atmospheric TRANsmission) model and converted to brightness temperatures by using the Planck law. We computed the Brightness Temperature Difference (BTD) between channels IR12.0 and IR10.8 to highlight the presence of ash/SO_2 plume, so we also computed the area of the volcanic cloud as seen from space for each image. In order to compare the temperature at the top of the volcanic cloud with the temperature of the atmospheric profile, we developed a MATLAB routine that interpolated the atmospheric profile at the measured value of temperature and provided the correspondent height. The interpolation is made through the MATLAB function *spline*. The method assumes that the top layer volcanic ash cloud behaves as a blackbody, and it is opaque; the assumption can cause significant overestimation of the cloud top temperature and, therefore, underestimation of the volcanic ash height if there are multilayer clouds under the top volcanic ash layer. Moreover, for high clouds near the tropopause and at high latitudes, the method can lead to errors because the rate of temperature change with height is small [73]. However, reanalysis of regional atmospheric products was used for ACTH estimations at the Etna volcano during recent eruptions [25,52]; the results of these models for lava fountains at Mount Etna were also validated with other ground-based approaches [59]. Finally, higher spatial resolution

images, such as those acquired by Sentinel-2 MSI, Landsat 8, and Aster, were used to locate and map the active or recently emplaced lava flow field [74,75].

2.3. High Precision Strain from the Borehole Dilatometer

A network composed of deep borehole dilatometers was installed on Etna in 2011 (two stations) and 2014 (further two stations). The dilatometers measure the volumetric strain of the rocks where they are installed, reaching nominal resolution of 10^{-10} to 10^{-11}, and guaranteeing a frequency range from 10^{-7} to >20 Hz. The instruments are usually installed into deep drilled holes (depth > 100 m) to reduce environmental noise, mainly the thermoelastic strain effects, to better exploit their high sensitivity. The instruments are coupled to the rock by using expansive cement and they require final calibration after installation. The calibrations are usually performed by comparing the recorded strain with the estimated reference signals, such as those produced by lunar tides, mainly the diurnal O1 (25.82 h) and the semidiurnal M2 (12.42 h) [58]. Other approaches are also implemented by comparing the recorded dynamic strain amplitude of long-period surface waves from strong distant earthquakes [76] or by direct comparison of the strain recorded by the borehole dilatometer with the seismic strain of teleseismic waves, recorded by a nearby broadband seismic array [77]. A detailed description of the installations, instrumental in situ calibrations, and main results are fully described by Bonaccorso et al. [76,78]. In this study, we used the signal from the most precise station, namely DRUV. This dilatometer was installed at a depth of 172.5 m within a very massive basalt layer in the mid-western flank of the volcano at about 10 km away from the summit craters (Figure 2). All previously cited calibration approaches were successfully applied to the strain recorded at this station obtaining the same calibration coefficient [58,76–78]. This is considered the reference station since, as testified by the in situ calibrations, it has a >20 times more precise sensitivity than the other stations.

3. Eruptive Activity before the 12 March 2021, Paroxysm

In the recent years, Etna volcano often displayed sequences of lava fountain events, mostly occurring from the SE Crater (SEC), and more recently from the NSEC [6,8,9,11,17]. These are characterized by the development of associated ash plumes and short-lived lava overflows from the crater rim [6–11,17]. Several periods of lava fountain activity characterized the growth of the SEC: in 1989 (16 lava fountains), in 1998–1999 (22), in 2000 (64), in 2001 (15), and in 2013–2015 (49) [8,14,15,17]. The first, most relevant of these sequences occurred in 2000, when during the six months (spanning between January and June) the SEC produced 64 such episodes [8]. This episodic activity was triggered by more primitive and gas-rich magma entering the SEC reservoir, where it mixed with the resident and more evolved magma, giving rise to a gas bubble foam layer accumulated at about 1.5 km depth below the erupting crater [7,8,57]. In general, paroxysmal episodes taking place close in time are generally impulsive and characterized by rapid waxing and waning phases compared to the episodes more distant in time that show a slower pattern [17].

Following the short flank eruption on Etna in December 2018 [25,27], the volcano had another effusive phase from the summit craters between 30 May and 6 June 2019, when some short fissures opened at the base of the NSEC, feeding a lava flow field that spread eastwards [26,79]. Once this eruptive activity ended, the summit craters of the volcano displayed a mild Strombolian explosive activity with occasional ash emission. On 18 July 2019, an effusive vent opened at the base of the NSEC, producing a small lava flow that spread NE for a few kilometers. This lava flow stopped on the evening of 20 July 2019. Another effusive vent opened on 27 July 2019, at the S base of the NSEC, producing a lava flow that spread towards SW and S for several hundred meters and stopped the next day. The Strombolian explosive activity at the summit craters continued during the year, accompanied by occasional and pulsating ash emissions, and producing an intra-crater cinder cone and a several hundred-meter-long lava flow within the Voragine crater in September 2019. From October 2019, the summit craters of the volcano displayed a mild

Strombolian explosive activity with occasional dilute ash emission [80]. In December 2019, the explosive activity increased in intensity, with bomb spatter and ballistics falling on the outer flanks of the NSEC, and a lava flow erupted from the Voragine crater, spreading within the nearby Bocca Nuova crater. This eruptive activity continued in 2020, intensifying during February–early March 2020 [80], when up to three scoria cones built up within the Voragine crater by March 2020. A complex lava flow field fed by the Voragine vents was spreading within the nearby Bocca Nuova crater, lasting until the end of April 2020. The Strombolian explosive activity continued at all summit craters with occasional dilute ash emissions, increasing in May 2020, and forming ash clouds rising several hundred meters above the craters. Several such ash clouds were also observed from June and August 2020 until 13 December 2020, when the first episode of lava fountaining occurred at the NSEC, accompanied by lava flow output from the crater rim spreading S. The collapse of a portion of the crater rim caused three pyroclastic density currents (PDC) spreading S, SW and SE from the base of the cone for several hundred meters. The explosive activity climaxed into an additional lava fountaining episode on 14 December 2020, and a lava flow from the NSEC spreading S on 15 December 2020. Additional lava fountaining episodes and lava flow outputs occurred on: 21 and 22 December 2020, 18 January 2021; on 16, 17, 19, 20, 22, 23, 24, and 28 February 2021; on 2, 4 (two episodes), 7, 9, 12, 14, 17, 19, 23, and 31 March 2021, on 19, 21, 22, 24, 25, 26 (three episodes), 27, 28 (four episodes), and 30 May 2021, on 2, 4, 12, 16, 17, 19, 20, 22, 23 (two episodes), 24, 25 (two episodes), 26, 27, and 28 June 2021; and on 1, 4, 6, 8, 14, 20 and 31 July 2021 (see activity reports of INGV-OE at https://www.ct.ingv.it/index.php/monitoraggio-e-sorveglianza/prodotti-del-monitoraggio/bollettini-settimanali-multidisciplinari, accessed on 2 August 2021).

4. Results

The chronology of the eruptive events was gathered from the analysis of the images acquired by the INGV monitoring network, comprising visible and thermal cameras (Table 1 and Figure 2) and allowing a view of the volcano from various distances and directions, and by satellite. All times indicated in this paper are UTC.

4.1. Eruptive Events and Characterization of the Lava Fountain and Ash Plume

The Strombolian activity at the NSEC, observed from the INGV network of monitoring cameras (Figure 2 and Table 1), started on 12 March 2021, at 02:35, gradually increasing in frequency, height, and intensity of the jets. Table 2 summarizes the timing of the events as observed by the monitoring cameras and satellite, also complemented by strain information. At 06:40 the activity became transitional between Strombolian and lava fountaining (Figure 3a), and at 07:00 a lava flow breached the lower eastern rim of the crater spreading E within the Valle del Bove depression (VdB; Figures 2 and 3b). At 07:22 a second overflow occurred from the NE margin of the crater rim, expanding on the N flank of the crater (Figure 3b). At 07:35, the explosive activity became a clear lava fountaining, accompanied by significant ash emission and fast formation and growth of an eruptive column (Figure 3b). The third lava flow started spreading SE from 09:20 (Figure 3c).

Table 2. Timing of the 12 March 2021, eruptive episode retrieved from the INGV monitoring cameras, from the satellite and strain signal. IER = instantaneous effusion rate [68].

| Time UTC	Eruptive Activity	Notes
02:35	Strombolian activity started at the NSEC	Figure 7
02:56	First satellite thermal anomaly detected and Strombolian activity intensified	Figure 7
05:00	Plume already reached 4000 m a.s.l.	Figures 5 and 6a
06:40	Transitional activity between Strombolian and lava fountaining started at NSEC	Figures 3a and 6b
07:00	Lava flow output started from the E rim of NSEC, expanding E	Figure 3a
07:22	A second lava flow started from the NE rim of NSEC, expanding N, strain suddenly declining	Figure 3b
07:35	Lava fountaining phase with significant ash emission and formation of an eruptive column, 20–30 m s-1 of muzzle velocity	Figures 3b and 6d
07:35–08:56	Radiant heat flux increased from satellite, muzzle velocity of ~70 m s-1, strain rate increased	Figure 9
08:14	Maximum muzzle velocity of 133 m s-1 reached by the lava fountain	
08:30	Maximum plume height of 11.3 km a.s.l. detected from EBVH	Figures 4 and 5
08:47–08:49	Maximum elevation reached by the lava fountain of 3000 m above the crater rim (from EBT), and of 2400 m above the crater rim (from ENT) and peak IER of 276 m3 s-1	Figures 4b and 5
08:57	Peak value of 35 GW measured from satellite and peak value from strain	Figures 5 and 9
09:05–09:30	The ash plume started declining in height	Figure 5
09:20	A third lava flow started from the SE rim of NSEC, expanding SE	Figure 3c
09:45	Lava fountain ended, strain declining stopped	Figure 3c
10:10–10:15	The ash plume dropped below 6.0 km a.s.l.	Figure 5
10:54	Explosive paroxysm ended	Figure 3c
12:00	Lava flow output ended and lava flow field cooling	
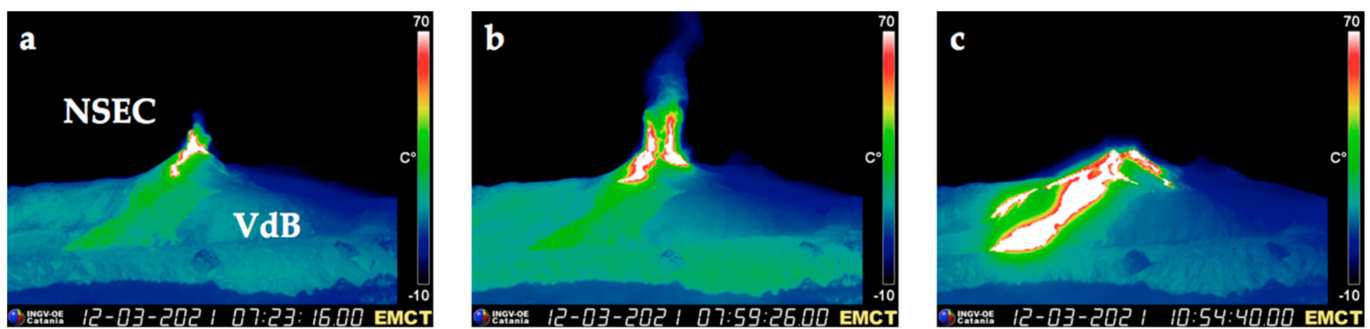
Figure 3. The output of three lava flows from the crater rim of the New Southeast Crater (NSEC), observed by the EMCT thermal camera located on the E flank of the volcano, on 12 March 2021. North is on the right, south is on the left. See Figure 2 for camera location and Table 1 for its characteristics. (**a**) Thermal image recorded at 07:23:16 showing the first lava flow (white) spreading E along the western wall of the Valle del Bove (VdB). (**b**) Thermal image recorded at 07:59:26 showing the lava fountain with the ash plume (blue), and the second lava flow spreading N (white, right of the image). (**c**) Thermal image recorded at 10:54:40 showing the crater inactive, and in white the three lava branches slowly expanding.

The height of the lava fountain, detected from the ENT (S flank) and EBT (NW flank, Figure 2 and Table 1) thermal cameras, gradually increased up to 08:49, when it reached the maximum elevation of 2400 m above the crater rim and the peak instantaneous effusion rate (IER, averaged over a shorter lapse of time than the effusion rate [68]) of 276 m^3 s^{-1} (Table 2). The muzzle velocity, obtained from the EMOT camera which is closer to the summit vents, was only 20–30 m s^{-1} during the initial phase of fountaining, increased to ~70 m s^{-1} after 08:05, and reached the peak of 133 m s^{-1} at 08:14 (Table 2). Then the fountain height decreased, stopping at 09:45 (Table 2), after a duration of 130 min (Figure 3). The average fountain height, calculated from the values measured every minute with the ENT camera, was 1149 m.

The height of the ash plume was measured on the frames overlapped on the visible images recorded by the ECV and EBVH visible cameras, located on the S and NW flank of the volcano, respectively (Figures 2 and 4, Table 1), using the calibrated images automatically provided by the procedure developed by Corradini et al. [59] and Scollo et al. [60,61]. The images of the ash plume are displayed in Figure 4, and the results of the ash plume heights against time are shown in Figure 5, where they are compared with the heights of the lava fountains retrieved from the ENT and EBT thermal cameras.
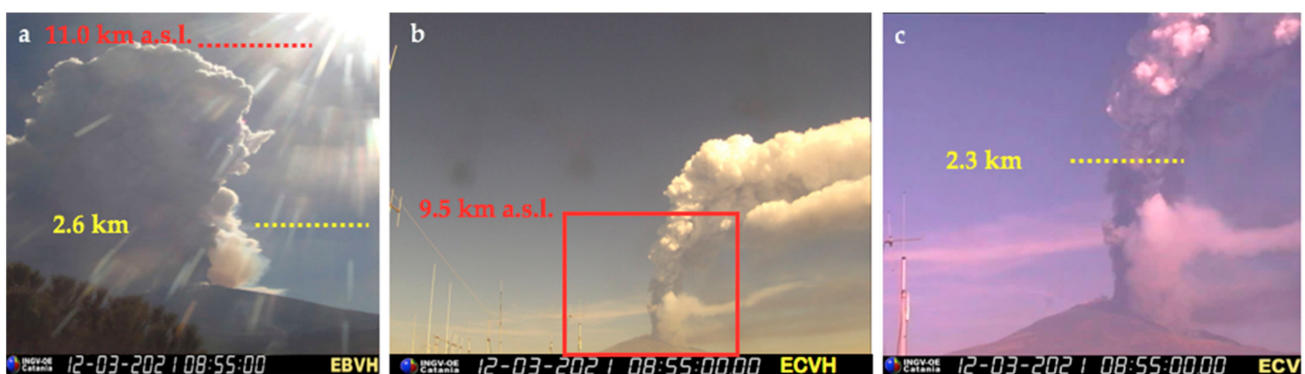

Figure 4. Heights and shapes of the 12 March 2021 ash plume at 08:55 imaged from (**a**) the EBVH calibrated camera located on the NW flank of the volcano where it reached 11.0 km above sea level (red dotted line) and with the lava fountain measuring 2.6 km above the crater rim (yellow dotted line), from (**b**) the uncalibrated ECVH camera located on the S flank of the volcano, with the red box displaying the area imaged in (**c**) and related to the ECV calibrated camera field of view, located in the same position as the ECVH, and having a maximum vertical field of view up to 9.5 km elevation above sea level, and displaying the elevation of the lava fountain (yellow dotted line) estimated at 2.3 km above the crater.
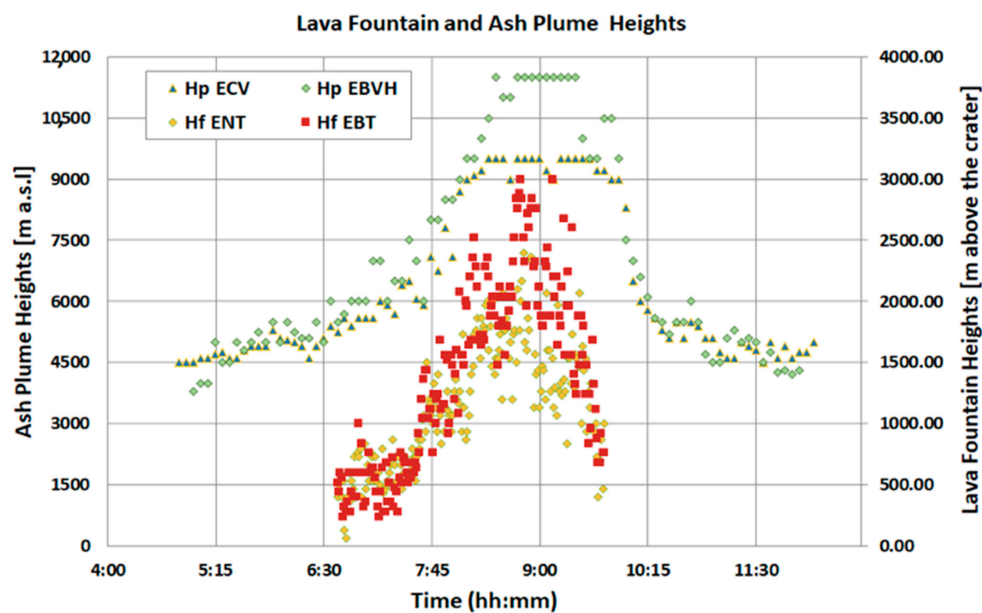
Figure 5. Heights of the lava fountain (Hf, in m above the crater rim) obtained from the ENT and the EBT thermal cameras, compared to the heights of the ash plume (Hp, in m above sea level) obtained from the ECV and EBVH visible cameras against time (hh:mm, UTC).

It is worth noting that although the lava fountain phase started at 07:35, the elevation of the plume was more than 4000 m above sea level (a.s.l.) much earlier, and at least from dawn at 05:00 when the ash plume became visible (Figures 5 and 6, Table 2). This was probably owing to the heat released by the Strombolian activity that started at the NSEC at 02:35 (Figure 3a and Table 2). However, at that time, it was a weak plume bent eastward and comprising mostly diluted reddish ash (Figure 6a). At 06:40, as soon as the explosive activity became transitional [4,14,43] between Strombolian and lava fountaining, the ash plume rose to 5300 m a.s.l. and changed inclination (Figure 6b), suddenly becoming more vertical as a result of an increased IER~120 $m^3 \ s^{-1}$ and displaying increasing water vapor condensation at the top (Figure 6c–e).
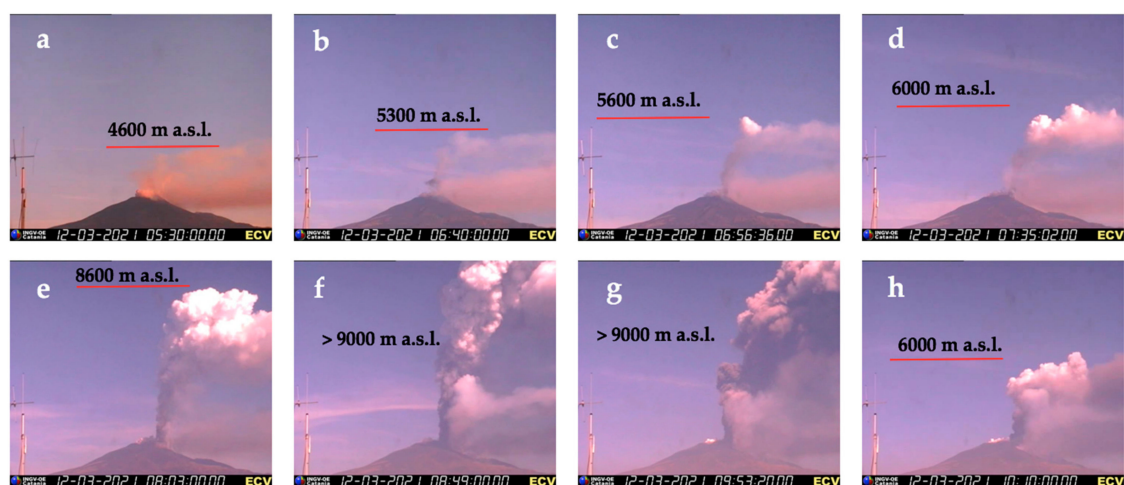

Figure 6. Heights and shapes of the 12 March 2021, ash plume imaged from the ECV calibrated camera. The vertical field of view reaches ~9.0 km above sea level. (**a**) Weak plume at 05:30; (**b**) weak ash plume at 06:40, with an upper part becoming more vertical; (**c**) intermediate ash plume at 06:56, with water vapor condensation at top; (**d**) intermediate ash plume at 07:35, when the lava fountain starts; (**e**) strong vertical plume at 08:03, slightly bent eastward (right) in the uppermost portion; (**f**) strong plume at 08:49, with a lower and more diluted cloud caused by the lava flow expanding eastward; (**g**) ash plume bending eastward after the end of the lava fountaining at 09:53; (**h**) ash plume decreasing in height at 10:10.

The amount of water vapor condensation at the top of the eruptive column increased even more after 07:35, when the eruptive activity became lava fountaining (Figure 6d–f). The increased IER~153 m^3 s^{-1} resulted in the formation of a strong plume extending vertically above the vent, with only the uppermost portion being bent eastward by the wind (Figure 6e). The ash plume went beyond the ECV camera field of view (i.e., more than 9.0–9.5 km a.s.l.) as soon as the lava fountain attained its peak IER of 252–276 m^3 s^{-1} at 08:47–08:49 (Table 2 and Figure 6f). At this stage, the lava flow field spreading eastward increased its speed significantly, as observed by satellite (Table 2) and also by the appearance of a lower steam cloud produced by the heat released by the lava flow (Figure 6f). The ash plume started to drop several minutes after the lava fountaining stopped (Figure 6g), but its disappearance was evident only after 10:10 (Figure 6h), about 30 min after the end of the lava fountaining phase.

The maximum plume elevation was not recorded by the ECV camera because its maximum field of view reaches ~9.0–9.5 km a.s.l. [60], but probably also the EBVH camera gave a slightly underestimated maximum ash plume elevation, given that the maximum elevation of 11.5 km a.s.l. was observed at 08:30 (Table 2 and Figure 5), whereas the maximum elevation of the lava fountains was attained at 08:49 from ENT (2.4 km above the crater rim, Table 2; average value 1.15 km).

The lava fountain heights decreased soon after having reached the peak values (i.e., at 08:50 from ENT; Figure 5), whereas the ash plume started decreasing in height at 09:05 from ECV and at 09:30 from EBVH, with a delay of 18–43 min (Figure 5).

Given that ash plume can be a serious threat to airport and airplane viability due to the proximity of Mount Etna with the Catania international airport (~32 km), we need to estimate the maximum elevation that the ash plume can attain, as well as its direction, as soon as possible, in order to provide prompt advice to the Civil Protection and Air Traffic Authorities. In this regard, the average lava fountain height is a key parameter because it allows us to estimate the maximum plume elevation as soon as the peak height of the lava fountain is reached. From the data recorded during the 2011–2013 lava fountains from NSEC, Calvari et al. [15] proposed the following empirical equation:

$$H_P = 5.26\, H_F + 6.83 \tag{2}$$

where H_P is the maximum height reached by the ash plume, and H_F is the average height of the lava fountain. Considering an average lava fountain height of 1.15 km above the crater rim, and applying the formula (2) by Calvari et al. [15], the estimated maximum plume height is 12.9 km, close to the real value of 11.5 km a.s.l. estimated from the EBVH monitoring camera (Figure 4a).

The difference in elevation for the lava fountain and ash plume obtained from the different cameras can be due to the irregular shapes of the lava fountain and ash plume, and/or to the ash partially obscuring the sight at the thermal image. Although the lava fountain suddenly stopped at 09:45, the ash plume was above 9.0 km a.s.l. at least for 10 additional minutes (until 09:55), and started to decrease below 6.0 km a.s.l. only after 10:10–10:15, with a delay of about 30 min (Figure 5).

On the basis of the lava fountain heights measured from the ENT camera, we estimated the volume of pyroclasts erupted during the lava fountain episode, following the method proposed by Calvari et al. [14,15]. The resulting volume is ~1.6 × 10^6 m^3, which, averaged over the 130 min of duration of the event, gave a time-averaged discharge rate (TADR; [68]) of ~209 m^3 s^{-1} and a peak instantaneous effusion rate (IER, [68]) of 276 m^3 s^{-1} recorded at 08:49.

4.2. Satellite Thermal Data

Processing satellite images enables us to derive: (i) the timing of eruptive activity as seen from space; an estimation of the (ii) area; and (iii) volume for the lava flow field and of (iv) the top height for the ash plume. The first thermal anomaly, related to the 12 March eruptive episode, was detected by SEVIRI at 02:56 when the Strombolian activity intensified

(Table 2). This anomaly was followed by a constant increase in the satellite-derived radiant heat flux mainly related to the lava flow spreading, as also visible from the lava flow area increase imaged by the EMCT thermal camera (Figure 7b). A first increase in the radiant heat flux signal was recorded at 6:42 and a second sharp increase occurred at 08:12, with a peak value of ~25 GW at 08:57 (Table 2). After this a constant decrease, related to the cooling of the lava flow, was observed. Due to the low spatial resolution of SEVIRI images at Etna volcano, we are not able to distinguish between the radiant heat flux curve coming from the lava fountain and the contribution related to the lava flow field. Most of the thermal signal is due to the lava flow emplacement as shown by the comparison with the lava flow field growth recorded by the EMCT thermal camera (Figure 7a,b). This happens for two reasons: the first is that the SEVIRI pixel over the summit crater saturates, and the second one is that the eruptive column above the lava fountain covers the view from the satellite. Applying the method by Ganci et al., [64], the satellite-derived cooling curve was modeled and a lava flow volume of ~2.4×10^6 m^3 was estimated.
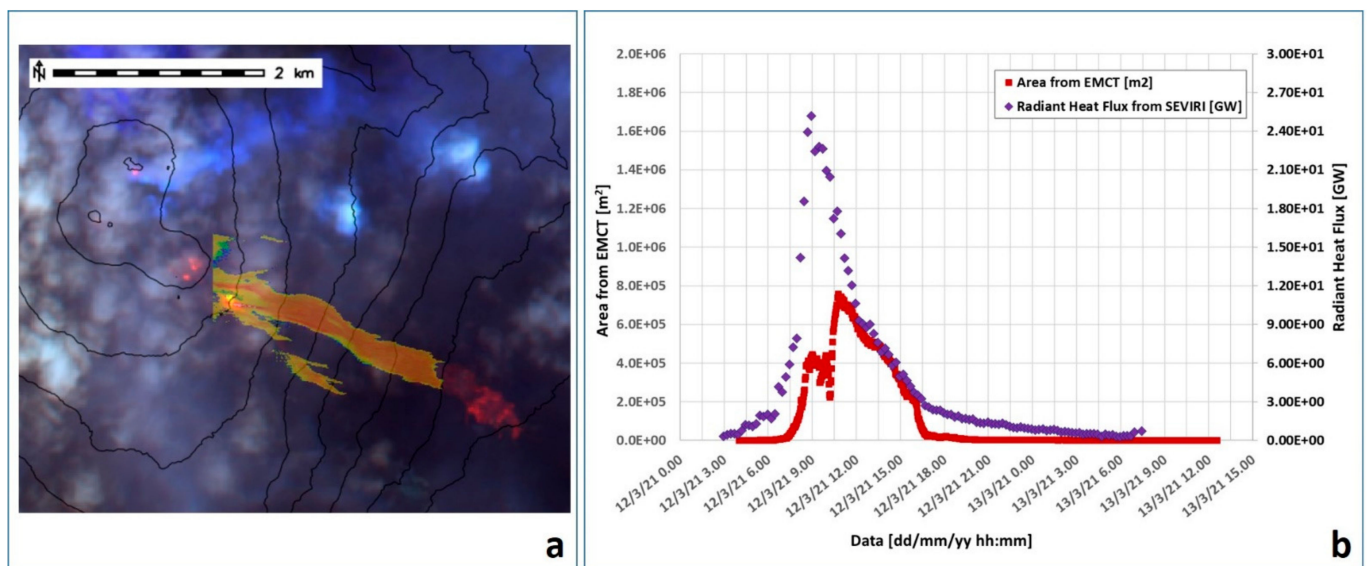

Figure 7. (**a**) Map of the lava flow derived from the thermal camera EMCT superimposed on the RGB composite (Band 12, Band 11, Band 5 at 20 m spatial resolution) of the Sentinel-2 image acquired on 13 March at 09:50. The projected map of the lava flow is cut in order to remove the jet portion of the lava fountain. (**b**) Thermally anomalous area detected from the EMCT thermal camera against time (red squares), compared with the radiant heat flux curve retrieved from SEVIRI (blue diamonds).

Figure 7b shows the SEVIRI-derived radiant heat flux versus the active lava flow area as imaged by the EMCT thermal camera. We found a slight difference between the two signals at the beginning and at the end because the oblique view from the camera missed the thermal activity at the crater area and part of the lava flow emplaced below ~1900 m a.s.l. that was instead visible by satellite. During the fountaining, the ash plume partially prevented the view of the lava flow field from EMCT (see Figure 6g,h), until 10:45 when the maximum value of 0.75×10^6 m^2 was reached. Figure 7a shows the lava flow area as imaged from EMCT superimposed on the RGB composite obtained from Band 12, Band 11, Band 5 (20 m spatial resolution) of the Sentinel-2 image acquired on 13 March at 09:50. The EMCT-derived map of the lava flow was retrieved considering all the images acquired by the camera with a portion of active lava flow from 12 March at 04:26 to 13 March at 05:40. We found an overlap of 97% between the projected thermal camera lava flow surface and the one visible from the Sentinel-2 image for the portion visible from the EMCT camera (Figure 7a). From the Sentinel-2 image, we derived a whole lava flow field area that resulted of about 1.17×10^6 m^2. Combining the SEVIRI-derived volume and the Sentinel-2 derived area, we found an average thickness of ~2.1 m for the lava flow field.

Figure 8 shows the ash cloud top height obtained from a VIIRS image acquired on 12 March 2021, at 10:46. The result is a maximum height of 12.6 km a.s.l. (Figure 8).
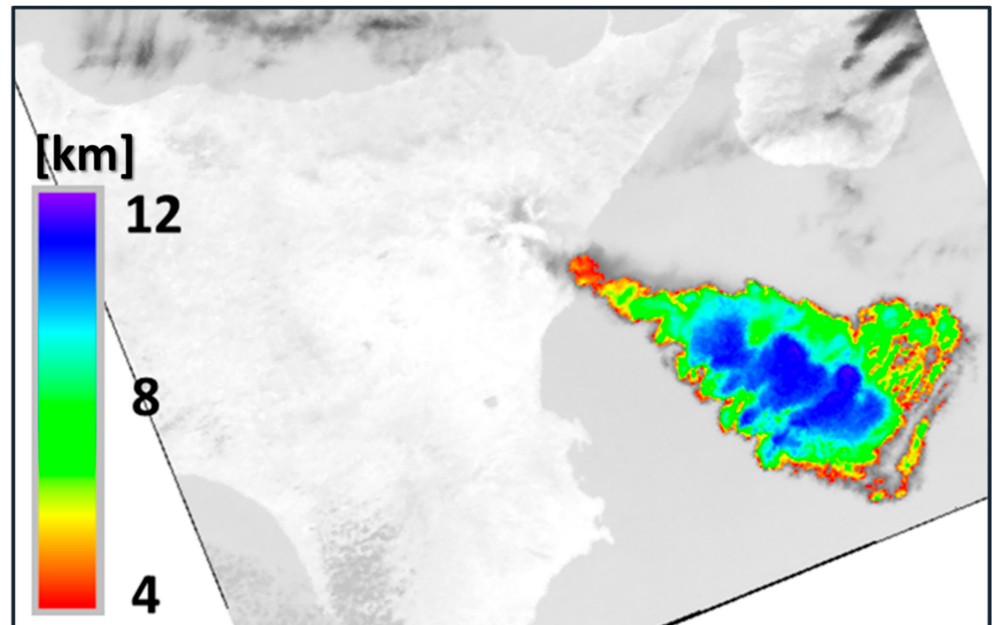

Figure 8. Ash Cloud Top Height (ACTH) computed from a VIIRS image of 12 March 2021, at 10:46.

By processing SEVIRI data, we were also able to follow the ash cloud dispersion during the eruptive episode. The plume top area was visible by SEVIRI at 8:15 and the area increased until 10:45 with an almost constant velocity between 0.1 and 0.2 km^2 s^{-1} (Figure 9). At 11:00, more than one hour after the end of the lava fountaining (Table 2), the plume top area started decreasing and separating from the volcano.
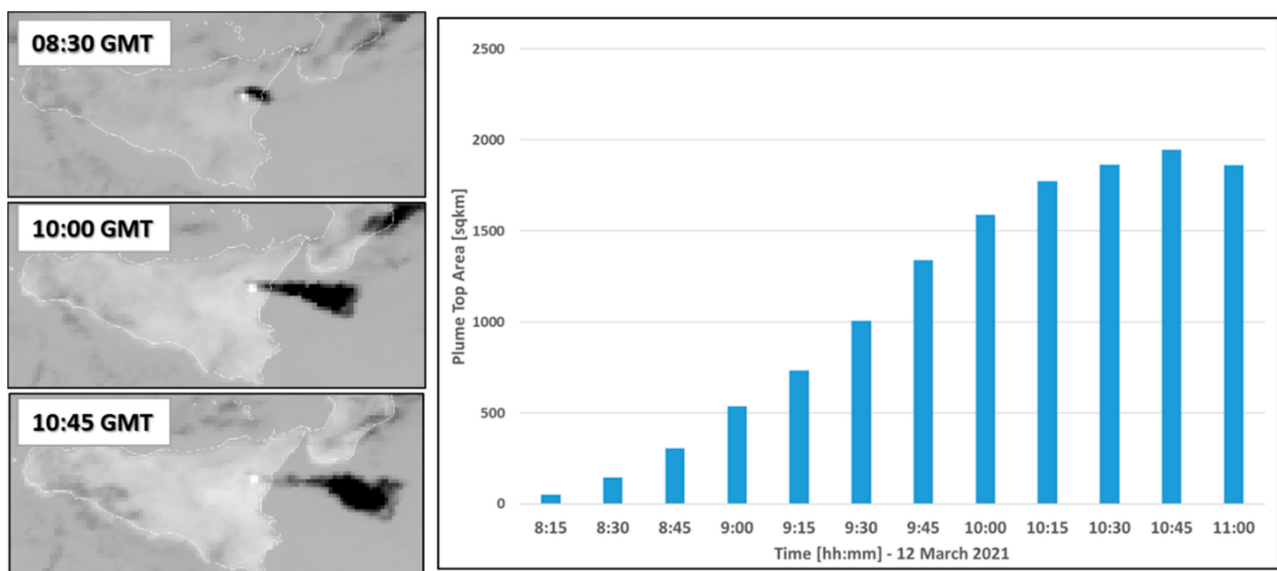

Figure 9. On the left: three SEVIRI scenes (channel IR 10.8) acquired on 12 March 2021 at 8:30, 10:00, and 10:45. On the right: histogram of the plume top area during 12 March 2021 from 8:15 to 11:00.

4.3. Strain

The DRUV reference station is located 10 km away from the summit craters (Figure 2), but has a very high sensitivity allowing to clearly detect the small strain variations (~0.2 microstrain) caused by the activity of the lava fountains at that distance. During the paroxysmal phase, the strain signal showed a negative variation which corresponded to a decompression of the medium surrounding the instrument. A weak variation started at 06:40, during the transitional phase (from Strombolian to lava fountaining activity) and the small lava flows occurrence. Then the strain increased its rate during the most intense lava fountain phase (07:35–08:57; Table 2). The strain signal continued to decrease until 09:46, cumulating a change of 0.18 microstrain. This variation is of the same order of magnitude as those recorded during the 2011–2013 paroxysmal episodes, with a value a little greater than the average of these events, which was 0.15 microstrain [58]. The strain rate, calculated as the strain change per 1 min sampling rate unit, reached a maximum value at 08:57. The strain recorded is shown in Figure 10a, where it is compared to the heat flux measured by satellite, and the strain rate against heat flux is shown in Figure 10b. In Figure 10, four phases can clearly be identified: (1) Strombolian activity and an initial weak effusive phase producing the beginning of the thermal release, but without strain change; (2) increase of the Strombolian activity (i.e., transitional activity between Strombolian and lava fountaining) in which the strain starts to decrease (i.e., decompression begins) and the strain rate increases; (3) start of the lava fountain phase ejecting at a high mass rate. This phase is characterized by a strong increment in the thermal contribution and by a marked decompression recorded by the strain. The maximum of the strain rate at 08:57 is coincident with the maximum of the radiant heat flux and lava fountain height (Table 2 and Figure 5); (4) after 08:56, the strain rate began to decrease, indicating that the lava fountain intensity was going to decrease and, therefore, the turning point of the strain rate represented the exact moment at which the eruptive activity started to decline; (5) at 09:45, the strain change reached the minimum, indicating that the lava fountain finished, the magma was no longer emitted, and the strain no longer recorded decompression (only the regular lunar tides), while the slow cooling of the hot material of the effused portion caused a slow exponential decrease in the thermal contribution detected by satellite.
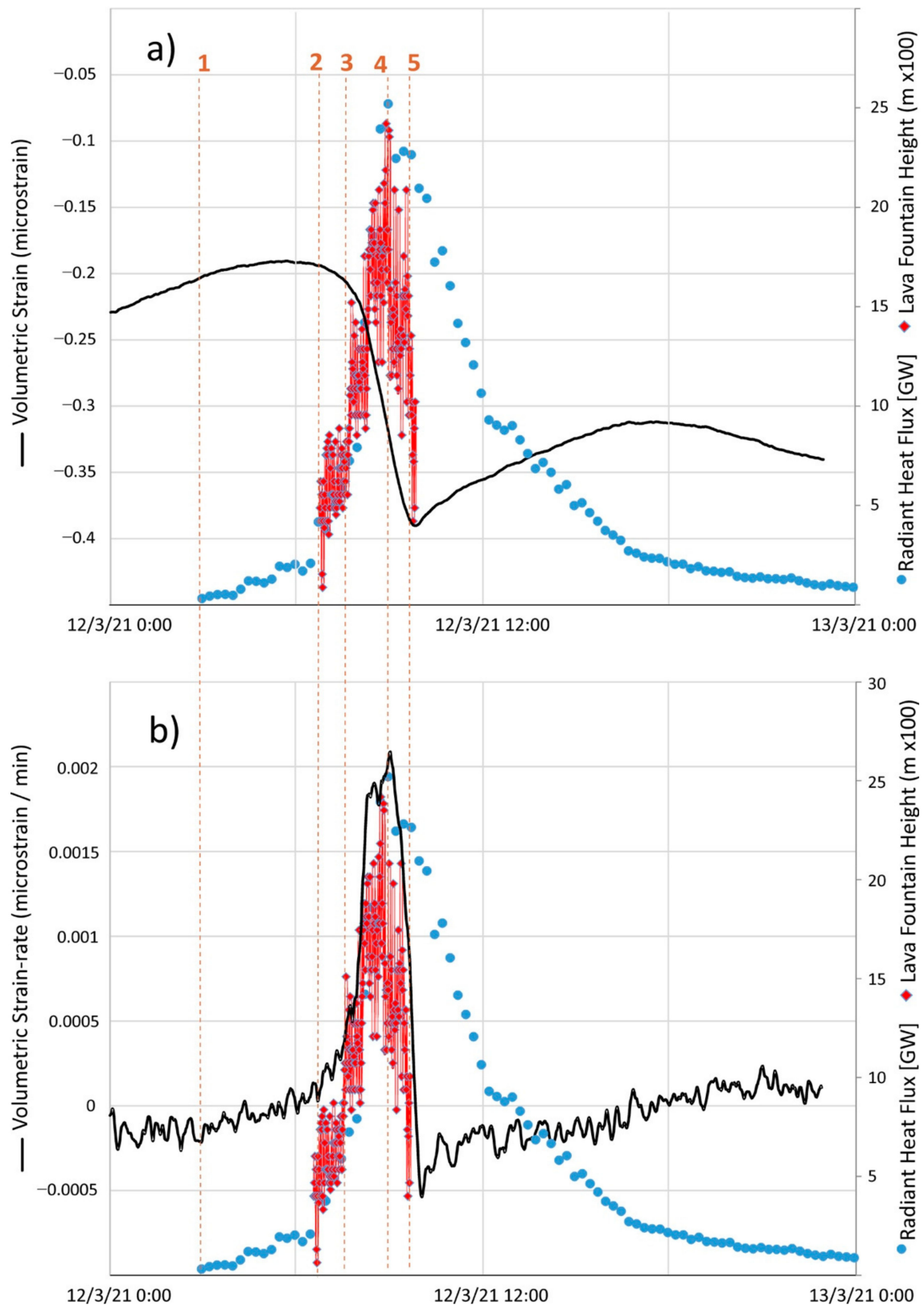
Figure 10. (**a**) Comparison of the radiant heat flux (GW, blue diamonds) detected by SEVIRI satellite with the strain signal (black line, in microstrain) and (**b**) the strain signal recorded at the DRUV station (black line, in microstrain per minute). (1) Strombolian activity and initial weak effusive phase; (2) transitional activity between Strombolian and lava fountaining; the strain starts to decrease and the strain rate increases; (3) start of the lava fountain phase; (4) the strain rate began to decrease indicating that the lava fountain intensity was going to decrease; (5) the strain change reached the minimum indicating that the lava fountain finished.

It is interesting to observe that the strain signal provided correct timings of the start and end of the lava fountain phase (Figure 10a), with times in agreement with those obtained from the camera frames. The strain rate marked the intensity regime of the explosive phase, and when the sign inversion occurred (at the beginning of phase 4, Figure 10a) there was a precise indication that the lava fountain began to decline (5, Figure 10b).

5. Discussion

The explosive mechanism of the lava fountains at Etna is generally understood as the "foam model" [81,82], which takes account of a rapid and violent ascent of a bubble foam layer previously accumulated at a shallow depth [7,8,14,83]. In this paper we have analyzed ground, satellite data and high precision strain signals collected during the 12 March lava fountain episode at Etna volcano in order to characterize the formation and growth of the lava fountain and of the associated lava flow field, and the way the fountain feeds the ash column and eruptive plume. The aim was to acquire parameters that could be useful for hazard assessment.

The cameras allowed us to observe the phenomenon from the ground and provided precise information on the characteristics of the lava fountain, on the subsequent eruptive column, ash plume development, and height. In particular, they constrained the total amount of the erupted fluid (gas plus pyroclasts) during the lava fountaining phase, and from this value we extracted the volume of pyroclasts as 0.18% of the total [14,15]. Thermal satellite analyses enable estimating the thermal energy and lava flows erupted during and after the lava fountains. In addition, satellite images reveal the size and elevation of the ash plume and their changes in time. The strain measures the response of the volcanic edifice to the decompression caused by the eruptive activity and provides constraints on the timing and total erupted volume. In general, the approach of integrating these various observations allowed us to obtain robust constraints to characterize the phenomenon.

In particular, in this study we have described the Strombolian activity at the vent, which began on 12 March 2021 at 02:35 (Table 2), gradually increasing with time in intensity and frequency of the bursts. Only after 06:40, i.e., after about 4 h of growing explosive activity, did the Strombolian activity pass to transitional explosions [14,39,43], and at 07:35, about one hour later, became lava fountaining. This transition corresponds to an increase in coalescence between gas bubbles [39] that drives the change from countable discrete explosions (Strombolian activity), revealing a bubbly flow regime within the conduit, to the transitional activity [14,39,43], indicative of a slug flow regime within the conduit, to the uncountable oscillations of a lava fountaining typical of a sustained annular flow regime [84]. It is at this stage—namely when lava fountaining is fully developed—that abundant ash is released from the fountain margins to feed the ash plume, suggesting further passage from an annular flow regime to a dispersed flow regime [84]. The lava fountaining phase showed a growing muzzle velocity that started from 20–30 m s^{-1}, rapidly grew to 70 m s^{-1}, and peaked at 133 m s^{-1} (Table 2). These values are in the range of Etna's previous paroxysmal events [15,31,85].

Considering that the wind speed during the lava fountaining episode ranged between ~5 and 10 m s^{-1}, at an altitude between 3 and 10 km (ERA5 Reanalysis available at https://cds.climate.copernicus.eu/, accessed on 2 August 2021), the results by Calvari et al. [15] is confirmed, namely that wind speed up to 10 m s^{-1} leads to a strong to intermediate plume rising vertically above the crater or slightly bending in the wind direction. This shape has a lower impact on the local population because ash fallout is mainly concentrated around the vent, but has a greater impact on aviation because the plume reaches greater elevation [15]. In the case of the 12 March 2021, paroxysmal episode, the ash plume rose to the maximum elevation of 11.3 km a.s.l. at 08:30, as detected from the monitoring cameras (Table 2), but grew even further away from the volcano and reached 12.6 km at 10:46 (Figure 8), as detected by the satellite. Thus, even more than one hour after the end of the lava fountaining, the ash plume was still threatening the airplanes path (Figures 8 and 9). Given that the maximum elevation of the lava fountaining was

detected 10–15 min after the top plume height detected from the EBVH camera (Table 2), it is possible that the maximum elevation of the ash plume was slightly higher than that detected by the EBVH ground camera even close to the volcano. This is confirmed by the 12.6 km detected by satellite at 10:46 (Figure 8) and is in agreement with what was predicted by the Equation (2) [15] that estimated a maximum ash plume elevation of 12.9 km.

The lava fountaining paroxysm ejected 1.6×10^6 m^3 pyroclasts at maximum IER of 276 m^3 s^{-1}. Most of the pyroclastic material erupted by the fountaining fell around the vent, further increasing the size of the NSEC cinder cone, as happened in the recent past [14,15,18,86]. Together with the lava fountaining, a lava flow also erupted from the crater rim, spreading a volume of 2.4×10^6 m^3 over a surface of 1.2×10^6 m^2 and travelling for 3.7 km eastward for a few hours.

The strain, based on the change cumulated during the lava fountain, was particularly useful for giving an estimate of the total erupted volumes, comprising both the pyroclasts erupted during the lava fountaining phase and the lava flows. In fact, considering the strain changes recorded during the lava fountains occurring at Etna on 2011–2013, Bonaccorso et al. [57] inferred a near spherical source of radius 0.5 km located below the crater area at a depth close to the sea level. This source represents the shallow storage where gas-rich magma is trapped and then violently ejected through the lava fountains. During the lava fountain, this source deflated and its volume changed by 2×10^6 m^3; due to the compressibility of the magma that accommodates a further amount of magma, the total volume of magma expelled was ~2.5×10^6 m^3 [57]. This was considered the representative volume for a lava fountain producing the mean strain change recorded for the 2011–2013 lava fountains, which was a 0.15 microstrain. Since the expected strain caused by a depressurizing spherical source is linearly related to the volume change of this source [87], we can use the results obtained by Bonaccorso et al. [57] to estimate the volume emitted by the NSEC lava fountains by the amplitude of the strain change at DRUV. For the 12 March 2021, episode, the 0.18 microstrain corresponds to a total emitted volume of ~3×10^6 m^3, comprising both lava flows and pyroclasts. This value results in an average eruption rate of 385 m^3 s^{-1}. However, by summing up the satellite-derived lava flow volume and the thermal camera derived pyroclastic volumes, a value of 4×10^6 m^3 is obtained. We argue that the lava fountain heights analysis measured a quantity of magma that partly flowed as lava flow and partly fell into the cone as pyroclasts. Indeed, by comparing the satellite-derived and the thermal camera derived volumes, the quantity of magma ejected into the fountain and falling into the lava flow field is about 1×10^6 m^3, while about 0.6×10^6 m^3 is related to pyroclasts. This value is comparable with the growth of the NSEC cone already measured during 2011–2013 [14], but also with a recent DEM difference computation by using Pleiades data (6.4×10^6 m^3 during 12 eruptive episodes; Ganci et al. unpublished data).

It is noteworthy that sustained ash plumes at the Etna volcano always accompany lava fountains [10,11,14,15,17,25,52–54,59]. Ash plumes cause the greatest concern on the civil protection authorities because they can attain up to 12–14 km in elevation [52,88] causing severe threat to the air traffic, while still expanding in the atmosphere, but also great damage to infrastructures, viability, and public health upon falling on the ground [30]. The ash plume forms as soon as the explosive activity shifts from transitional to lava fountain (stage 3 in Figure 10), most often within 30 min from the paroxysmal start [14,15,25]. It corresponds to an acceleration of the jet that is responsible for the peak IER (Table 2) and the greater cooling and fragmentation of pyroclasts [25,33,44]. The heat released during the lava fountain phase is sufficient to rise a large volume of fine-grained pyroclasts (ash) up into the atmosphere, causing it to spread for several hours around the volcano, and to travel distances of several tens of kilometers [89].

A numerical study involving explosive eruptions, carried out at the Etna volcano [90], estimated that the mass deposited over a distance of 1 and 100 km from the vent represents 30% of the emitted pyroclastic mass. Thus, it is noteworthy that this amount was sufficient to feed an ash plume 11–13 km high (Table 2, Figures 4 and 5) expanding for hundreds of

kilometers from the vent (Figures 8 and 9), and covering a sky surface of up to 1900 km^2 and a distance of ~140 km from the vent in two and half hours. This matches a plume-cloud expanding for 60 km from the vent in just 50 min during a previous paroxysmal episode [89], and fully displays the hazard posed by the ash cloud to aviation safety and circulation also because of growing airline traffic [91–93]. It is, thus, of paramount importance to use monitoring data to develop simple equations, such as those used during recent effusive eruptions at Etna [94,95], which might allow for fast and reliable estimates useful for hazard assessment during the earlier phases of an explosive paroxysm. In this respect, application of the formula proposed by Calvari et al. [15], to estimate the maximum vertical extent of the ash plume once the lava fountaining phase stabilized, proved to be effective when applied to the 12 March 2021, paroxysm. In fact, this formula estimated an ash plume maximum elevation of 12.9 km a.s.l., which is a value very close to the 12.6 km a.s.l. estimated from the satellite images.

6. Conclusions

Our results have essential implications in regard to hazard assessments at Etna during paroxysmal explosive phases. They confirm the role of wind speed [15] in determining if a strong, intermediate, or weak ash plume forms, with wind speeds below 10 m s^{-1} favoring the formation of strong to intermediate, taller vertical plumes, which cause most of the pyroclastic fallout around the vent. Our results on the 12 March 2021, episode confirm the possibility of estimating the maximum ash plume elevation using the formula proposed by Calvari et al. [15], given that the maximum plume elevation obtained by satellite (12.6 km) was very close to the 12.9 km estimated by the empirical formula. Integrating results from the ground monitoring cameras, satellite, and strainmeters, we obtained an estimation of the total erupted volume of 3×10^6 m^3, of which 1.6×10^6 m^3 erupted as pyroclasts, with ~1×10^6 m^3 of the volume of pyroclasts flowing together with the lava flows to comprise a lava flow field extending over a surface of ~1.17×10^6 m^2, with a volume of 2.4×10^6 m^3. Considering the duration of 130 min for the episode, there was an average eruption rate of 385 m^3 s^{-1} for this event, comprising both pyroclasts and lava flows. Our results show that extreme caution must be applied when calculating the volume erupted during paroxysmal episodes, combining data obtained from monitoring cameras and satellites. In fact, by comparing these results with the strain changes at the shallow magma source, we have shown how a significant portion of pyroclasts (~1×10^6 m^3) flowed along the flanks of the NSEC cone to feed the lava flows. This corresponds to ~33% of the total volume erupted by the paroxysmal episode.

Although the duration of the eruptive event was rather short (130 min), the expansion of the ash cloud continued for the following hours, reaching the maximum elevation detected by satellite about 1 h after the end of the paroxysm (Figures 8 and 9). The ash cloud expanded in the atmosphere and eventually detached from the volcano 1.5 h after the end of the paroxysm (Figure 9). This result must be taken into account when organizing air traffic immediately after the end of an explosive paroxysm.

Author Contributions: Conceptualization, S.C.; methodology, S.C., G.G., A.B.; validation, S.C., G.G., A.B.; formal analysis, S.C., G.G., A.B.; investigation, S.C., G.G., A.B.; resources, S.C.; data curation, S.C., G.G., A.B.; visible and thermal ground imagery data treatment, S.C., G.G.; satellite data treatment, G.G.; ground deformation data treatment, A.B.; writing—original draft preparation, S.C., G.G., A.B.; writing—review and editing, S.C., G.G., A.B.; visualization, S.C., G.G., A.B.; supervision, S.C., G.G., A.B.; project administration, S.C.; funding acquisition, S.C. All authors have read and agreed to the published version of the manuscript.

References

1. Wilson, L.; Parfitt, E.A.; Head, J.W., III. Explosive volcanic eruptions-VIII. The role of magma recycling in controlling the behaviour of Hawaiian-style lava fountains. *Geophys. J. Int.* **1995**, *121*, 215–225. [CrossRef]
2. Swanson, D.A.; Duffield, W.A.; Jackson, D.B.; Peterson, D.W. *Chronological Narrative of the 1969–71 Mauna Ulu Eruption of Kilauea Volcano, Hawai'i*; U.S. Geological Survey Professional Paper 1056; U.S. Government Printing Office: Washington, DC, USA, 1979.
3. Wolfe, E.W.; Neal, C.A.; Banks, N.G.; Duggan, T.J. Geological observations and chronology of eruptive events. In *The Puu Oo eruption of Kilauea Volcano, Hawaii*; Episodes 1 through 20, January 3, 1983, through June 8, 1984; U.S. Geological Survey Professional Paper 1463; U.S. Government Printing Office: Washington, DC, USA, 1988.
4. Parfitt, E.A.; Wilson, L. The 1983–86 Pu'u'O'o eruption at Kilauea Volcano, Hawaii: A study of dike geometry and eruption mechanisms for a long-lived eruption. *J. Volcanol. Geotherm. Res.* **1994**, *59*, 179–205. [CrossRef]
5. Parcheta, C.E.; Houghton, B.F.; Swanson, D.A. Contrasting patterns of vesiculation in low, intermediate, and high Hawaiian fountains: A case study of the 1969 Mauna Ulu eruption. *J. Volcanol. Geotherm. Res.* **2013**, *255*, 79–89. [CrossRef]
6. Alparone, S.; Andronico, D.; Lodato, L.; Sgroi, T. Relationship between tremor and volcanic activity during the Southeast Crater eruption on Mount Etna in early 2000. *J. Geophys. Res.* **2003**, *108*, B52241. [CrossRef]
7. Allard, P.; Burton, M.; Murè, F. Spectroscopic evidence for a lava fountain driven by previously accumulated magmatic gas. *Nature* **2005**, *433*, 407–410. [CrossRef] [PubMed]
8. Andronico, D.; Corsaro, R.A. Lava fountains during the episodic eruption of South–East Crater (Mt. Etna), 2000: Insights into magma-gas dynamics within the shallow volcano plumbing system. *Bull. Volc.* **2011**, *73*, 1165–1178. [CrossRef]
9. Behncke, B.; Neri, M. The July-August 2001 eruption of Mt. Etna (Sicily). *Bull. Volcanol.* **2003**, *65*, 461–476. [CrossRef]
10. Andronico, D.; Branca, S.; Calvari, S.; Burton, M.R.; Caltabiano, T.; Corsaro, R.A.; Del Carlo, P.; Garfi, G.; Lodato, L.; Miraglia, L.; et al. A multi-disciplinary study of the 2002–03 Etna eruption: Insights for into a complex plumbing system. *Bull. Volcanol.* **2005**, *67*, 314–330. [CrossRef]
11. Andronico, D.; Scollo, S.; Caruso, S.; Cristaldi, A. The 2002–03 Etna explosive activity: Tephra dispersal and features of the deposits. *J. Geophys. Res.* **2008**, *113*, B04209. [CrossRef]
12. Bonaccorso, A.; Calvari, S. A new approach to investigate an eruptive paroxysmal sequence using camera and strainmeter networks: Lessons from the 3–5 December 2015 activity at Etna volcano. *Earth Plan. Sci. Lett.* **2017**, *475*, 231–241. [CrossRef]
13. Bonaccorso, A.; Calvari, S.; Linde, A.; Sacks, S. Eruptive processes leading to the most explosive lava fountain at Etna volcano: The 23 November 2013 episode. *Geophys. Res. Lett.* **2014**, *41*, 4912–4919. [CrossRef]
14. Calvari, S.; Salerno, G.G.; Spampinato, L.; Gouhier, M.; La Spina, A.; Pecora, E.; Harris, A.J.L.; Labazuy, P.; Biale, E.; Boschi, E. An unloading foam model to constrain Etna's 11–13 January 2011 lava fountaining episode. *J. Geophys. Res.* **2011**, *116*, B11207. [CrossRef]
15. Calvari, S.; Cannavò, F.; Bonaccorso, A.; Spampinato, L.; Pellegrino, A.G. Paroxysmal Explosions, Lava Fountains and Ash Plumes at Etna Volcano: Eruptive Processes and Hazard Implications. *Front. Earth Sci.* **2018**, *6*, 107. [CrossRef]

16. Ganci, G.; Cappello, A.; Bilotta, G.; Herault, A.; Zago, V.; Del Negro, C. Mapping volcanic deposits of the 2011–2015 Etna Eruptive events using satellite remote sensing. *Front. Earth Sci.* **2018**, *6*, 83. [CrossRef]

17. Andronico, D.; Cannata, A.; Di Grazia, G.; Ferrari, F. The 1986–2021 paroxysmal episodes at the summit craters of Mt. Etna: Insights into volcano dynamics and hazard. *Earth Sci. Rev.* **2021**, *220*, 103686. [CrossRef]

18. Behncke, B.; Stefano Branca, S.; Corsaro, R.A.; De Beni, E.; Miraglia, L.; Proietti, C. The 2011–2012 summit activity of Mount Etna: Birth, growth and products of the new SE crater. *J. Volcanol. Geoth. Res.* **2014**, *270*, 10–21. [CrossRef]

19. Andronico, D.; Scollo, S.; Cristaldi, A.; Lo Castro, M.D. Representativity of incompletely sampled fall deposits in estimating eruption source parameters: A test using the 12–13 January 2011 lava fountain deposit from Mt. Etna volcano, Italy. *Bull. Volcanol.* **2014**, *76*, 861. [CrossRef]

20. Wadge, G.; Guest, J.E. Steady-state magma discharge at Etna 1971–81. *Nature* **1981**, *294*, 548–550. [CrossRef]

21. Harris, A.J.L.; Steffke, A.; Calvari, S.; Spampinato, L. Thirty years of satellite-derived lava discharge rates at Etna: Implications for steady volumetric output. *J. Geophys. Res.* **2011**, *116*, B08204. [CrossRef]

22. Bonaccorso, A.; Calvari, S. Major effusive eruptions and recent lava fountains: Balance between erupted and expected magma volumes at Etna volcano. *Geophys. Res. Lett.* **2013**, *40*, 6069–6073. [CrossRef]

23. Bonaccorso, A.; Aloisi, M. Tracking magma storage: New perspectives from 40 years (1980–2020) of ground deformation source modeling on etna volcano. *Front. Earth Sci.* **2021**, *9*, 638742. [CrossRef]

24. Aloisi, M.; Bonaccorso, A.; Cannavò, F.; Currenti, G.; Gambino, S. The 24 December 2018 eruptive intrusion at Etna volcano as revealed by multidisciplinary continuous deformation networks (CGPS, borehole strainmeters and tiltmeters). *J. Geophys. Res.* **2020**, *125*, e2019JB019117. [CrossRef]

25. Calvari, S.; Bilotta, G.; Bonaccorso, A.; Caltabiano, T.; Cappello, A.; Corradino, C.; Del Negro, C.; Ganci, G.; Neri, M.; Pecora, E.; et al. The VEI 2 Christmas 2018 Etna eruption: A small but intense eruptive event or the starting phase of a larger one? *Remote Sens.* **2020**, *12*, 905. [CrossRef]

26. De Beni, E.; Cantarero, M.; Neri, M.; Messina, A. Lava flows of Mt Etna, Italy: The 2019 eruption within the context of the last two decades (1999–2019). *J. Maps.* **2020**, *17*, 65–76. [CrossRef]

27. Mattia, M.; Bruno, V.; Montgomery-Brown, E.; Patanè, D.; Barberi, G.; Coltelli, M. Combined seismic and geodetic analysis before, during, and after the 2018 Mount Etna eruption. *Geochem. Geophys. Geosyst.* **2020**, *21*, e2020GC009218. [CrossRef]

28. Kampouri, A.; Amiridis, V.; Solomos, S.; Gialitaki, A.; Marinou, E.; Spyrou, C.; Georgoulias, A.K.; Akritidis, D.; Papagiannopoulos, N.; Mona, L. Investigation of Volcanic Emissions in the Mediterranean: "The Etna–Antikythera Connection". *Atmosphere* **2021**, *2*, 40. [CrossRef]

29. Wilson, T.M.; Cole, J.W.; Stewart, C.; Cronin, S.J.; Johnston, D.M. Ash storms: Impacts of wind-remobilised volcanic ash on rural communities and agriculture following the 1991 Hudson eruption, southern Patagonia, Chile. *Bull. Volc.* **2011**, *73*, 223–239. [CrossRef]

30. Andronico, D.; Del Carlo, P. PM10 measurements in urban settlements after lava fountain episodes at Mt. Etna, Italy: Pilot test to assess volcanic ash hazard to human health. *Nat. Hazards Earth Syst. Sci. Discuss.* **2016**, *16*, 29–40. [CrossRef]

31. Donnadieu, F.; Freville, P.; Hervier, C.; Coltelli, M.; Scollo, S.; Prestifilippo, M.; Valade, S.; Rivet, S.; Cacault, P. Near-source Doppler radar monitoring of tephra plumes at Etna. *J. Volcanol. Geotherm. Res.* **2016**, *312*, 26–39. [CrossRef]

32. Marzano, F.S.; Mereu, L.; Scollo, S.; Donnadieu, F.; Bonadonna, C. Tephra Mass Eruption Rate From Ground-Based X-Band and L-Band Microwave Radars During the November 23, 2013, Etna Paroxysm. *IEEE Trans. Geosci. Rem. Sens.* **2020**, *58*, 3314–3327. [CrossRef]

33. Patrick, M.R.; Harris, A.J.L.; Ripepe, M.; Dehn, J.; Rothery, D.; Calvari, S. Strombolian explosive styles and source conditions: Insights from thermal (FLIR) video. *Bull. Volcanol.* **2007**, *69*, 769–784. [CrossRef]

34. Murata, K.J.; Dondoli, C.; Saenz, R. The 1963–65 eruption of Irazú Volcano, Costa Rica (the period of March 1963 to October 1964). *Bull. Volcanol.* **1966**, *29*, 765–796. [CrossRef]

35. Booth, B.; Walker, G.P.L. Ash deposits from the new explosion crater, Etna 1971. *Trans. R. Soc. Lond.* **1973**, *A274*, 147–161.

36. Taddeucci, J.; Pompilio, M.; Scarlato, P. Conduit processes during the July–August 2001 explosive activity of Mt Etna (Italy): Inferences from glass chemistry and crystal size distribution of ash particles. *J. Volcanol. Geotherm. Res.* **2004**, *137*, 33–54. [CrossRef]

37. Lautze, N.; Houghton, B.F. Physical mingling of magma and complex eruption dynamics in the shallow conduit at Stromboli Volcano, Italy. *Geology* **2005**, *33*, 425–428. [CrossRef]

38. Head, J.W.; Wilson, L. Lava fountain heights at Pu'u O'o, Kilauea, Hawaii: Indicators of amount and variations of ex- solved magma volatiles. *J. Geophys. Res.* **1987**, *92*, 13715–13719. [CrossRef]

39. Parfitt, E.A.; Wilson, L.; Neal, C.A. Factors influencing the height of Hawaiian lava fountains: Implications for the use of fountain height as an indicator of magma gas content. *Bull. Volcanol.* **1995**, *57*, 440–450. [CrossRef]

40. Walker, G.P.L. Explosive volcanic eruptions—a new classification scheme. *Geol. Rundsch.* **1973**, *62*, 431–446. [CrossRef]

41. Parfitt, E.A. A study of clast size distribution, ash deposition and fragmentation in a Hawaiian-style volcanic eruption. *J. Volcanol. Geotherm. Res.* **1998**, *84*, 197–208. [CrossRef]

42. Sparks, R.S.J.; Bursik, M.I.; Carey, S.N.; Gilbert, J.S.; Glaze, L.S.; Sigurdsson, H.; Woods, A.W. *Volcanic Plumes*; John Wiley Sons: Hoboken, NJ, USA, 1997; p. 574. ISBN 0-471-93901-3.

43. Spampinato, L.; Calvari, S.; Oppenheimer, C.; Lodato, L. Shallow magma transport for the 2002–03 Mt. Etna eruption inferred from thermal infrared surveys. *J. Volcanol. Geotherm. Res.* **2008**, *177*, 301–312. [CrossRef]

44. Taddeucci, J.; Pompilio, M.; Scarlato, P. Monitoring the explosive activity of the July–August 2001 eruption of Mt. Etna (Italy) by ash characterization. *Geophys. Res. Lett.* **2002**, *29*, 71-1–71-4. [CrossRef]

45. Dellino, P.; Kyriakopoulos, K. Phreatomagmatic ash from the ongoing eruption of Etna reaching the Greek island of Cefalonia. *J. Volcanol. Geotherm. Res.* **2003**, *126*, 341–345. [CrossRef]

46. Calvari, S.; Pinkerton, H. Birth, growth and morphologic evolution of the "Laghetto" cinder cone during the 2001 Etna eruption. *J. Volcanol. Geotherm. Res.* **2004**, *132*, 225–239. [CrossRef]

47. Calvari, S.; Pinkerton, H. Instabilities in the summit region of Mount Etna during the 1999 eruption. *Bull. Volcanol.* **2002**, *63*, 526–535. [CrossRef]

48. Andronico, D.; Spinetti, C.; Cristaldi, A.; Buongiorno, M.F. Observations of Mt. Etna volcanic ash plumes in 2006: An integrated approach from ground-based and polar satellite NOAA–AVHRR monitoring system. *J. Volcanol. Geotherm. Res.* **2009**, *180*, 135–147. [CrossRef]

49. Harris, D.M.; Rose, W.I. Estimating particle size, concentrations, and total mass of ash in volcanic clouds using weather radar. *J. Geoph. Res.* **1983**, *88*, 10969–10983. [CrossRef]

50. Spinetti, C.; Barsotti, S.; Neri, A.; Buongiorno, M.F.; Doumaz, F.; Nannipieri, L. Investigation of the complex dynamics and structure of the 2010 Eyjafjallajokull volcanic ash cloud using multispectral images and numerical simulations. *J. Geophys. Res. Atmos.* **2013**, *118*, 4729–4747. [CrossRef]

51. Durig, T.; Gudmundsson, M.T.; Karmann, S.; Zimanowski, B.; Dellino, P.; Rietze, M.; Buttner, R. Mass eruption rates in pulsating eruptions estimated from video analysis of the gas thrust-buoyancy transition—A case study of the 2010 eruption of Eyjafjallajökull, Iceland. *Earth Planets Space* **2015**, *67*, 180. [CrossRef]

52. Corradini, S.; Montopoli, M.; Guerrieri, L.; Ricci, M.; Scollo, S.; Merucci, L.; Marzano, F.S.; Pugnaghi, S.; Prestifilippo, M.; Ventress, L.J.; et al. Multi-Sensor Approach for volcanic ash cloud retrieval and eruption characterization: The 23 November 2013 Etna Lava Fountain. *Remote Sens.* **2016**, *8*, 58. [CrossRef]

53. Corradini, S.; Guerrieri, L.; Stelitano, D.; Salerno, G.; Scollo, S.; Merucci, L.; Prestifilippo, M.; Musacchio, M.; Silvestri, M.; Lombardo, V.; et al. Near real-time monitoring of the Christmas 2018 Etna eruption using SEVIRI and products validation. *Remote Sens.* **2020**, *12*, 1336. [CrossRef]

54. Corradini, S.; Guerrieri, L.; Brenot, H.; Clarisse, L.; Merucci, L.; Pardini, F.; Prata, A.J.; Realmuto, V.J.; Stelitano, D.; Theys, N. Tropospheric volcanic SO$_2$ mass and flux retrievals from satellite. The Etna December 2018 eruption. *Remote Sens.* **2021**, *13*, 2225. [CrossRef]

55. Athanassiadou, M. The Mt Etna SO$_2$ eruption in December 2015—The view from space. *Weather* **2016**, *71*, 273–278. [CrossRef]

56. Bluth, G.J.S.; Doiron, S.D.; Schnetzler, C.C.; Krueger, A.J.; Walter, L.S. Global tracking of the SO2 cloud from the June, 1991 Mount Pinatubo eruptions. *Geophys. Res. Lett.* **1992**, *19*, 151–154. [CrossRef]

57. Bonaccorso, A.; Calvari, S.; Currenti, G.; Del Negro, C.; Ganci, G.; Linde, A.; Napoli, R.; Sacks, S.; Sicali, A. From source to surface: Dynamics of Etna's lava fountains investigated by continuous strain, magnetic, ground and satellite thermal data. *Bull. Volcanol.* **2013**, *75*, 690. [CrossRef]

58. Bonaccorso, A.; Currenti, G.; Linde, A.; Sacks, S. New data from borehole strainmeters to infer lava fountain sources (Etna 2011–2012). *Geophys. Res. Lett.* **2013**, *40*, 3579–3584. [CrossRef]

59. Corradini, S.; Guerrieri, L.; Lombardo, V.; Merucci, L.; Musacchio, M.; Prestifilippo, M.; Scollo, S.; Silvestri, M.; Spata, G.; Stelitano, D. Proximal monitoring of the 2011–2015 Etna lava fountains using MSG-SEVIRI data. *Geosciences* **2018**, *8*, 140. [CrossRef]

60. Scollo, S.; Prestifilippo, M.; Pecora, E.; Corradini, S.; Merucci, L.; Spata, G.; Coltelli, M. Eruption column height estimation of the 2011–2013 Etna lava fountains. *Ann. Geophys.* **2014**, *57*, S0214.

61. Scollo, S.; Prestifilippo, M.; Bonadonna, C.; Cioni, R.; Corradini, S.; Degruyter, W.; Rossi, E.; Silvestri, M.; Biale, E.; Carparelli, G.; et al. Near-real-time tephra fallout assessment at Mt. Etna, Italy. *Remote Sens.* **2019**, *11*, 2987. [CrossRef]

62. Ganci, G.; James, M.R.; Calvari, S.; Del Negro, C. Separating the thermal fingerprints of lava flows and simultaneous lava fountaining using ground-based thermal camera and SEVIRI measurements. *Geophys. Res. Lett.* **2013**, *40*, 5058–5063. [CrossRef]

63. Corradino, C.; Ganci, G.; Cappello, A.; Bilotta, G.; Calvari, S.; Del Negro, C. Recognizing eruptions of mount etna through machine learning using multiperspective infrared images. *Remote Sens.* **2020**, *12*, 970. [CrossRef]

64. Ganci, G.; Vicari, A.; Cappello, A.; Del Negro, C. An emergent strategy for volcano hazard assessment: From thermal satellite monitoring to lava flow modelling. *Remote Sens. Environ.* **2012**, *119*, 197–207. [CrossRef]

65. Ganci, G.; Harris, A.J.L.; Del Negro, C.; Guéhenneux, Y.; Cappello, A.; Labazuy, P.; Calvari, S.; Gouhier, M. A year of lava fountaining at Etna: Volumes from SEVIRI. *Geophys. Res. Lett.* **2012**, *39*, L06305. [CrossRef]

66. Ganci, G.; Vicari, A.; Fortuna, L.; Del Negro, C. The HOTSAT volcano monitoring system based on combined use of SEVIRI and MODIS multispectral data. *Ann. Geophys.* **2011**, *54*, 5. [CrossRef]

67. Ganci, G.; Cappello, A.; Bilotta, G.; Corradino, C.; Mangiameli, M.; Mussumeci, G.; Del Negro, C. 3D Lava flow mapping in volcanic areas using multispectral and stereo optical satellite data. *AIP Conf. Proc.* **2020**, *2293*, 300003. [CrossRef]

68. Harris, A.J.L.; Dehn, J.; Calvari, S. Lava effusion rate definition and measurement: A review. *Bull. Volcanol.* **2007**, *70*, 1–22. [CrossRef]

69. Harris, A.J.L.; Flynn, L.P.; Keszthelyi, L.; Mouginis-Mark, P.J.; Rowland, S.K.; Resing, J.A. Calculation of lava effusion rates from Landsat TM data. *Bull. Volcanol.* **1998**, *60*, 52–71. [CrossRef]

70. Wright, R.; Blake, S.; Harris, A.; Rothery, D. A simple explanation for the space-based calculation of lava eruption rates. *Earth Plan. Sci. Lett.* **2001**, *192*, 223–233. [CrossRef]

71. Garel, F.; Kaminski, E.; Tait, S.; Limare, A. An experimental study of the surface thermal signature of hot subaerial isoviscous gravity currents: Implications for thermal monitoring of lava flows and domes. *J. Geophys. Res.* **2012**, *117*, B02205. [CrossRef]

72. Hon, K.; Kauahikaua, J.; Denlinger, R.; Mackay, K. Emplacement and inflation of pahoehoe sheet flows: Observations and measurements of active lava flows on Kilauea Volcano, Hawaii. *Geol. Soc. Am. Bull.* **1994**, *106*, 351–370. [CrossRef]

73. Prata, A.J.; Bluth, G.J.S.; Rose, W.I.; Schneider, D.J.; Tupper, A.C. Comments on failures in detecting volcanic ash from a satellite-based technique. *Remote Sens. Environ.* **2001**, *78*, 341–346. [CrossRef]

74. Del Negro, C.; Cappello, A.; Ganci, G. Quantifying lava flow hazards in response to effusive eruption. *Geol. Soc. Am.* **2015**, *128*, 752–763. [CrossRef]

75. Corradino, C.; Ganci, G.; Cappello, A.; Bilotta, G.; Herault, A.; Del Negro, C. Mapping recent lava flows at Mount Etna using multispectral sentinel-2 images and machine learning techniques. *Remote Sens.* **2019**, *11*, 1916. [CrossRef]

76. Bonaccorso, A.; Linde, A.; Currenti, G.; Sacks, S.; Sicali, A. Theborehole dilatometer network of Mount Etna: A powerful tool to detect and infer volcano dynamics. *J. Geophys. Res. Solid Earth* **2016**, *121*, 4655–4669. [CrossRef]

77. Currenti, G.; Zuccarello, L.; Bonaccorso, A.; Sicali, A. Borehole volumetric strainmeter calibration from a nearby seismic broadband array at Etna volcano. *J. Geophys. Res.* **2017**, *122*, 7729–7738. [CrossRef]

78. Bonaccorso, A.; Currenti, G.; Linde, A.; Sacks, S.; Sicali, A. Advances in understanding intrusive, explosive and effusive processes as revealed by the borehole dilatometer network on Mt. Etna volcano. *Front. Earth Sci.* **2020**, *7*, 357. [CrossRef]

79. Marchese, F.; Neri, M.; Behncke, B. Main morpho-structural changes and eruptions of Etna in 2016–2019 captured by satellite observations. In Proceedings of the 22nd EGU General Assembly, Online Event, 4–8 May 2020; p. EGU2020-13909. [CrossRef]

80. Genzano, N.; Marchese, F.; Neri, M.; Pergola, N.; Tramutoli, V. Implementation of robust satellite techniques for volcanoes on ASTER data under the google earth engine platform. *Appl. Sci.* **2021**, *11*, 4201. [CrossRef]

81. Jaupart, C.; Vergniolle, S. Laboratory models of Hawaiian and Strombolian eruptions. *Nature* **1988**, *331*, 58–60. [CrossRef]

82. Jaupart, C.; Veirgniolle, S. The generation and collapse of foam layer at the roof of a basaltic magma chamber. *J. Fluid Mech.* **1989**, *203*, 347–380. [CrossRef]

83. Bonaccorso, A.; Cannata, A.; Corsaro, R.A.; Di Grazia, G.; Gambino, S.; Greco, F.; Miraglia, L.; Pistorio, A. Multi-disciplinary investigation on a lava fountain preceding a flank eruption: The 10 May 2008 Etna case. *Geochem. Geophys. Geosyst.* **2011**, *12*, 7. [CrossRef]

84. Jaupart, C. Magma ascent at shallow levels. *Encycl. Volcanoes* **1999**, *1*, 237–245.

85. Dubosclard, G.; Cordesses, R.; Allard, P.; Hervier, C.; Coltelli, M.; Kornprobst, J. First testing of a volcano Doppler radar (Voldorad) at Mt. Etna. *Geophys. Res. Lett.* **1999**, *26*, 3389–3392. [CrossRef]

86. De Beni, E.; Behncke, S.; Branca, I.; Nicolosi, R.; Carluccio, F.; D'Ajello, C.; Chiappini, M. The continuing story of Etna's new southeast crater (2012–2014): Evolution and volume calculations based on field surveys and aerophotogrammetry. *J. Volcanol. Geotherm. Res.* **2015**, *303*, 175–186. [CrossRef]

87. Roeloffs, E.A.; Linde, A.T. Borehole observations and continuous strain and fluid pressure. In *Volcano Deformation Geodetic Measurments Techniques*; Dzurisin, D., Ed.; Springer: Berlin/Heidelberg, Germany, 2007; pp. 305–322. [CrossRef]

88. Vulpiani, G.; Ripepe, M.; Valade, S. Mass discharge rate retrieval combining weather radar and thermal camera observations. *J. Geophys. Res. Solid Earth* **2016**, *121*, 5679–5695. [CrossRef]

89. Pailot-Bonnétat, S.; Harris, A.J.L.; Calvari, S.; De Michele, M.; Gurioli, L. Plume height time-series retrieval using shadow in single spatial resolution satellite images. *Remote Sens.* **2020**, *12*, 3951. [CrossRef]

90. Spanu, A.; de'Michieli Vitturi, M.; Barsotti, S. Reconstructing eruptive source parameters from tephra deposit: A numerical study of medium-sized explosive eruptions at Etna volcano. *Bull. Volcanol.* **2016**, *78*, 59. [CrossRef]

91. Casadevall, T.J. Volcanic ash and aviation safety: Proceedings of the First International Symposium on Volcanic Ash and Aviation Safety. *USGS Bull.* **1994**, *2047*, 450–469.

92. Rose, W.I.; Delene, D.J.; Schneider, D.J.; Bluth, G.J.S.; Krueger, A.J.; Sprod, I.; McKee, C.; Davies, H.L.; Erns, G.G.J. Ice in the 1994 Rabaul eruption cloud: Implications for volcano hazard and atmospheric effects. *Nature* **1995**, *375*, 477–479. [CrossRef]

93. Marzano, F.S.; Picciotti, E.; Montopoli, M.; Vulpiani, G. Inside Volcanic Clouds. Remote Sensing of Ash Plumes Using Microwave Weather Radars. *Am. Meteorol. Soc.* **2013**, *94*, 1567–1586. [CrossRef]

94. Bonaccorso, A.; Calvari, S.; Boschi, E. Hazard mitigation and crisis management during major flank eruptions at Etna volcano: Reporting on real experience. In *Detecting, Modelling and Responding to Effusive Eruptions*; Harris, A.J.L., De Groeve, T., Garel, F., Carn, S.A., Eds.; Special Publications (IAVCEI) Series; Geological Society of London: London, UK, 2015; Volume 426, pp. 447–461. ISBN 978-1-86239-736-1. [CrossRef]

95. Solana, M.C.; Calvari, S.; Kilburn, C.R.J.; Gutierrez, H.; Chester, D.; Duncan, A. Supporting the development of procedures for communications during volcanic emergencies: Lessons learnt from the Canary Islands (Spain) and Etna and Stromboli (Italy). In *Advances in Volcanology, Observing the Volcano World, Volcano Crisis Communication*; Fearnley, C.J., Bird, D.K., Haynes, K., McGuire, W.J., Jolly, G., Eds.; Springer: Cham, Switzerland, 2017; pp. 289–305. ISBN 978-3-319-44095-8. [CrossRef]